Journal of Materials Chemistry A

PAPER

View Article Online
View Journal | View Issue

Cite this: J. Mater. Chem. A, 2019, 7, 14816

The synergistic effect of cation mixing in mesoporous $Bi_xFe_{1-x}VO_4$ heterojunction photoanodes for solar water splitting†

Mengyuan Zhang,[a] Huu Khue Pham,[a] Yanan Fang,[a] Ying Fan Tay,[a] Fatwa F. Abdi *[b] and Lydia H. Wong *[a]

Mixed metal vanadates are an interesting class of materials due to their favorable bandgap for visible light absorption and their catalytic activity. Here, we report a novel $Bi_xFe_{1-x}VO_4$ mixture system fabricated by electrospinning, which upon annealing is composed of triclinic $FeVO_4$ and monoclinic $BiVO_4$ phases. The mixture demonstrates extended optical absorption and a clear bandgap shift as compared with a pure $BiVO_4$. This is also accompanied by an extended wavelength range for its photoactivity as evident from the incident photon-to-current efficiency. In addition, the mixture with a Bi/(Bi + Fe) ratio of 0.5 (*i.e.*, $x = 0.5$) shows superior charge transfer and charge separation efficiency. The improved charge transfer efficiency is attributed to the higher catalytic activity of the mixed cation, while the presence of a $BiVO_4/FeVO_4$ heterojunction enhances the charge separation. The formation of the heterojunction is verified through detailed microscopic investigations revealing $BiVO_4$ particles intimately surrounded by $FeVO_4$. Our results demonstrate the advantage of establishing a mixture of complex metal oxides in extending optical absorption and boosting the photoelectrochemical performance.

Received 17th February 2019
Accepted 16th May 2019

DOI: 10.1039/c9ta01791g

rsc.li/materials-a

Introduction

In the field of photoelectrochemical (PEC) water splitting, bismuth vanadate ($BiVO_4$) has emerged as one of the highest performing metal oxide photoanodes. With recent progress and success of achieving 90% of its theoretical maximum photocurrent, it is clear that further improvement in the solar-to-hydrogen (STH) efficiency of bismuth vanadate ($BiVO_4$) is limited by its bandgap (2.4–2.5 eV).[1,2] Numerous attempts have been reported on either identifying novel narrow bandgap photoanode materials or decreasing the bandgap of $BiVO_4$. Some emerging materials, such as $CuWO_4$ (2.1 eV),[3] $SnWO_4$ (2.1 eV),[4,5] $ZnFe_2O_4$ (2.0 eV),[6,7] $Cu_xV_yO_z$ (1.8–2.0 eV),[8,9] and $FeVO_4$ (2.06 eV),[10,11] have been reported to be promising photoanode candidates. However, these novel complex metal oxides still show much lower performance than expected, and further developments on a relatively longer timescale are necessary. Sulfurization or nitridation has been demonstrated to effectively reduce the bandgap of $BiVO_4$, but its PEC stability may be a concern.[2,12] As an alternative, the bandgap of $BiVO_4$ can also be modified by incorporating another metal cation to form a metal vanadate mixture. The combination of a new metal cation—if chosen properly—could possibly raise the valence band of $BiVO_4$ without much effect on the conduction band or form a favorable heterojunction with extended light absorption. The effective bandgap, as a result, will be reduced.

Studies on mixed metal vanadates have been reported from a decade ago for photocatalytic applications (*e.g.*, $BiCu_2VO_6$ and $BiZn_2VO_6$).[13–18] Combining two metal vanadates (Cu and Bi) into a solid solution to lower the bandgap of $BiVO_4$ has been experimentally demonstrated.[13,15] The absorption of $BiCu_2VO_6$ extends to 600 nm, which is 80 nm longer than that of $BiVO_4$. It was proposed that the bandgap reduction is due to band modulation through the incorporation of two metal cations. The additional advantage reported is that $BiCu_2VO_6$ and $BiZn_2VO_6$ possess higher photocatalytic activity than pristine $BiVO_4$.[15,17] Similarly, a $Bi_{0.75}Fe_{0.25}VO_4$ mixture demonstrated higher photocatalytic efficiency in the degradation of methylene blue than $FeVO_4$ or $BiVO_4$.[19] However, the detailed mechanism on why mixed vanadates can offer higher catalytic activity or improved photoelectrochemical performance is not well understood. In addition, a high performance mixed vanadate photoanode has not been reported in the literature.

In our previous report, a series of $Bi_xFe_{1-x}VO_4$ ($0 \leq x \leq 1$) films were fabricated by spray pyrolysis.[20] Initial results indicated the possibility of maintaining good mobility of $BiVO_4$ and extending visible light absorption by mixing $FeVO_4$ with $BiVO_4$. The present study adopts electrospinning to deposit mixed

[a]School of Materials Science and Engineering, Nanyang Technological University, Nanyang Avenue, Singapore 639798. E-mail: lydiawong@ntu.edu.sg
[b]Institute for Solar Fuels, Helmholtz-Zentrum Berlin für Materialien und Energie GmbH, Hahn-Meitner-Platz 1, Berlin 14109, Germany. E-mail: fatwa.abdi@helmholtz-berlin.de

† Electronic supplementary information (ESI) available. See DOI: 10.1039/c9ta01791g

vanadate films and higher annealing temperature to improve the crystallinity. The combination of Fe and Bi vanadate shows higher catalytic efficiency and increased visible light absorption; in particular, the $Fe_{0.5}Bi_{0.5}VO_4$ composition demonstrates the highest PEC performance. Microscopic observations show that the $Fe_{0.5}Bi_{0.5}VO_4$ consists of adjacent $FeVO_4$ and $BiVO_4$ nanoparticles, which results in a favorable heterojunction to facilitate charge separation. Our study presents the synergistic effect of a Bi/Fe vanadate heterojunction and gives insights to further improve the performance of vanadate-based photoanodes.

Results and discussion

Physical characterization and chemical compositions

We prepared a series of $Bi_xFe_{1-x}VO_4$ ($0 \leq x \leq 1$) films by electrospinning (Scheme S1†) (the expression $Bi_xFe_{1-x}VO_4$ here is determined by the composition of precursors and does not necessarily indicate the formation of a solid solution). For brevity, the different films are denoted by the percentage amount of Bi in each film, *i.e.*, Bi0 corresponds to a $FeVO_4$ film, Bi50 corresponds to $Bi_{0.5}Fe_{0.5}VO_4$, and Bi100 corresponds to $BiVO_4$. Prior to other measurements, EDX spectroscopy was used to confirm that the Fe and Bi ratio follows the initial amount added to the precursor (Fig. 1a). EDX mapping confirms the uniform distribution of Fe and Bi throughout the film (Fig. S1†). Fig. 1b shows the X-ray diffraction (XRD) patterns of the various $Bi_xFe_{1-x}VO_4$ films. At each extreme of the composition (*i.e.*, Bi0 and Bi100), a pure phase of triclinic $FeVO_4$ and monoclinic $BiVO_4$ was obtained, respectively. For the mixed vanadate, both $FeVO_4$ and $BiVO_4$ peaks were detected from Bi5 to Bi50. From Bi65 and above, the $FeVO_4$ phase can no longer be detected by XRD, but only the $BiVO_4$ peak intensity changes with increasing Bi content (Fig. S2†). This may be caused by the relatively small amount of $FeVO_4$ phase in the films. Further investigations on the crystal structure by transmission electron microscopy are discussed later in the paper. Compared with the peak intensity of $BiVO_4$, the $FeVO_4$ peak intensity is relatively lower. This is due to the fact that the films were annealed at 550 °C while annealing at 650 °C is typically required to obtain good crystallinity of $FeVO_4$.[10,20] This lower temperature was chosen as a compromise because V loss occurs at temperatures above 450 °C.[21] Fig. S3† indeed shows that all of our films are slightly V-poor. The effect of V loss has been discussed elsewhere and is not the focus of this report.[21]

The chemical composition and oxidation states in the films were analyzed by XPS. All the spectra were calibrated using the adventitious carbon peak at 284.8 eV. Fe, Bi, V and O core level XPS spectra of $FeVO_4$, Bi50 and $BiVO_4$ films are shown in Fig. S4.† Peaks at 710–714 eV can be observed in $FeVO_4$ and Bi50 films, which can be assigned to Fe $2p_{3/2}$ multiplets with an oxidation state of +3.[22,23] The peak at 716 eV, which is present for all films, corresponds to the Sn $3p_{3/2}$ core level, which is caused by the exposed FTO.[24] XPS peaks at 158.7 eV and 164.1 eV confirm the existence of Bi^{3+} in Bi50 and $BiVO_4$.[25,26] The vanadium is present as V^{5+} in all films, as evident from the V $2p_{3/2}$ peak at ~516.9 eV.[27,28] The binding energy of O 1s at 530 eV matches with the oxygen lattice peak in the oxide.[27] The peak positions do not shift for all films, suggesting that the chemical environment of the mixture remains unchanged.

A gradual color change from orange ($FeVO_4$) to bright yellow ($BiVO_4$) can be observed in the visual appearance of the films (Fig. S5†), similar to our previous report.[20] The porous appearance of the films is due to the addition of PVP to the electrospinning precursor. The absorption spectra of the mixed vanadate films obtained from UV-vis spectroscopy are shown in Fig. 2a and b. Other than the pure $BiVO_4$ film, the absorption edge of the mixed vanadate films extends beyond 520 nm (absorption edge of $BiVO_4$), validating the effect of Fe incorporation on increasing the visible light absorption range. For Bi10 to Bi50 films, a higher Bi ratio increases the absorption at around 480 nm, which is a characteristic absorption shoulder of $BiVO_4$ (Fig. 2a). Beyond this Bi concentration (*i.e.*, 50% and above), visible light absorption at the 520–600 nm range decreases with higher Bi content (Fig. 2b), possibly due to the difference of absorption coefficients of $BiVO_4$ and $FeVO_4$.[20,29]

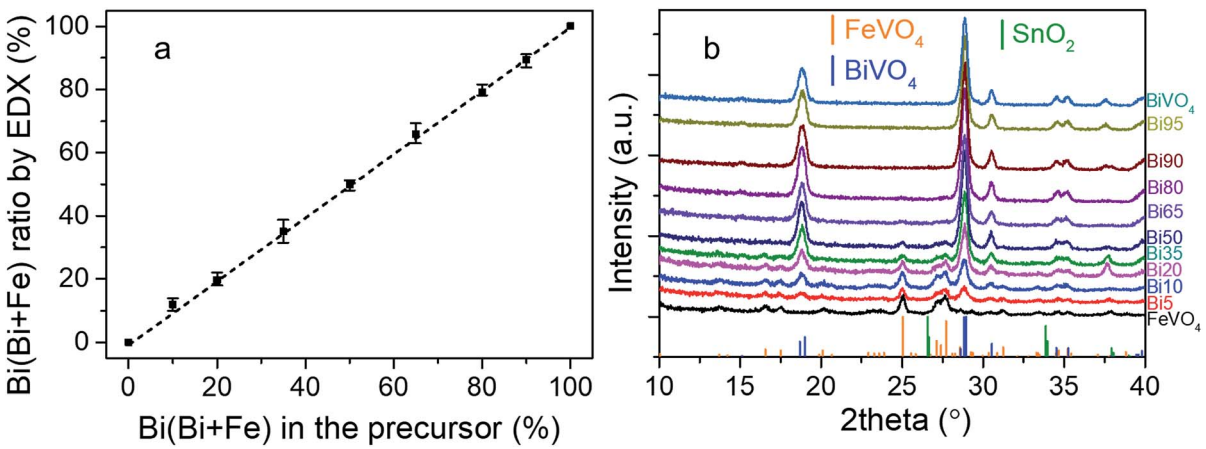

Fig. 1 (a) Bi ratio in the annealed films calculated from the EDX results compared with the Bi ratio in the precursor. (b) XRD patterns of all compositions annealed at 550 °C in air.

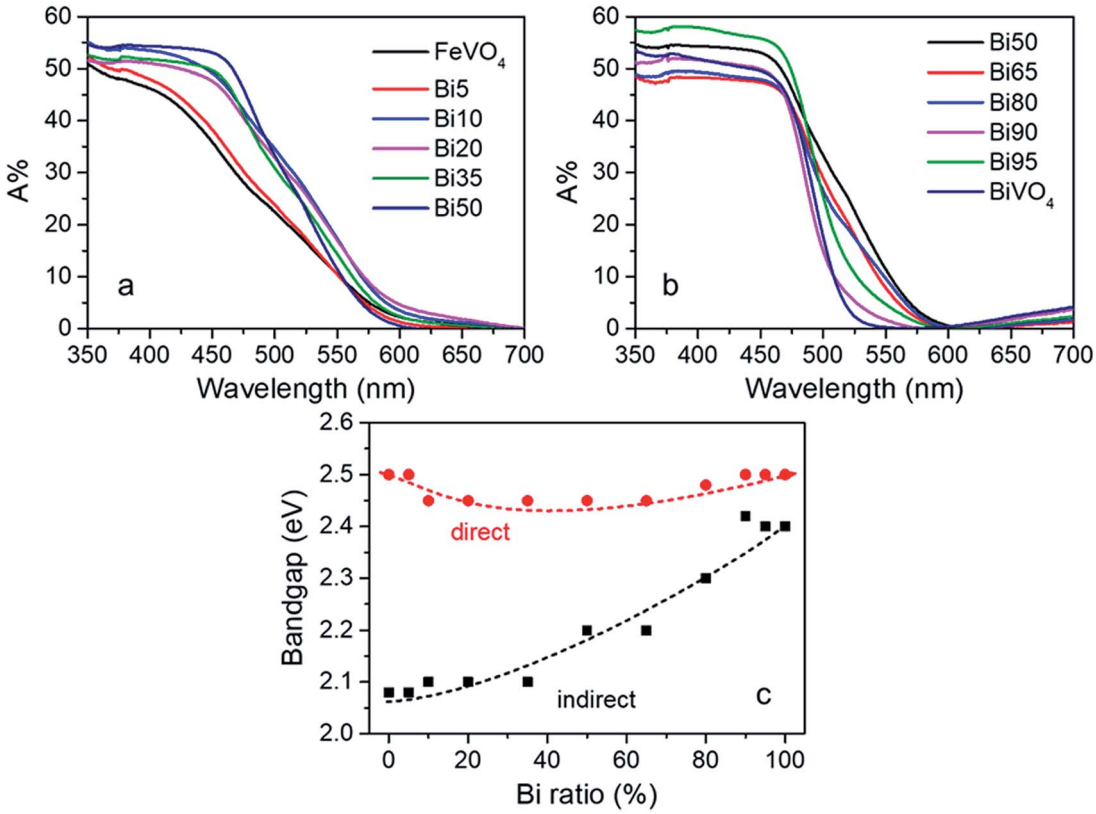

Fig. 2 (a) and (b) Absorption spectra and (c) calculated direct and indirect bandgaps for all films with various Bi ratios.

Although the films were detected to be mixtures of $BiVO_4$ and $FeVO_4$, the 'apparent bandgap' of the mixture, instead of the actual bandgap, can still be determined. Thus, the direct and indirect bandgaps of all the films can be calculated using Tauc analysis; the results are shown in Fig. 2c. The direct bandgap only shows minor differences for all compositions (2.45–2.5 eV), but the indirect bandgap increases with increasing Bi content.

Our results clearly show that a higher Fe content leads to a larger visible absorption range. However, the appearance of the absorption shoulder at 480 nm and the varying absorption spectra at ~520–600 nm suggest that an optimal Bi/Fe ratio may exist in order to achieve the maximum total absorption. By integrating all the absorption spectra with the AM1.5 photons, the theoretical absorbed photocurrent density (J_{abs}) can be readily calculated for each composition and the results are shown in Fig. S6.† All the films have a J_{abs} of ~3–4 mA cm^{-2}. With these absorption changes brought about by the Bi/Fe ratio, a maximum is observed for the Bi10 film (4 mA cm^{-2}).

Improved charge carrier efficiencies

The AM1.5 photocurrent density of all films was measured in 0.1 M phosphate buffer (KPi, pH = 7). Most films show higher photocurrent under back-side illumination as compared to front illumination (Fig. S7†). 30 min deposition time (electrospinning) is found to be optimal to ensure sufficient film thickness and avoid delamination of films during annealing. As the PEC performance is similar for 30 min and 45 min deposited films (Fig. S8†), only films electrospun for 30 minutes will be discussed below (the original photocurrent curves are shown in Fig. S9†). As shown in Fig. 3a, the photocurrent of pristine $FeVO_4$ and $BiVO_4$ is quite comparable to the previously reported sprayed $FeVO_4$ and electrospun $BiVO_4$.[20,27] The comparison of the photocurrents for the electrospun and spray pyrolysed samples are shown in Table S1.† Among all the compositions, the Bi50 film shows the highest photocurrent (0.47 mA cm^{-2} at 1.23 V *vs.* RHE). The peak photocurrent trend at a Bi 50% ratio is even more obvious at higher potential, while other Bi rich or Fe rich composition films only generate moderate photocurrents. From Bi0 to Bi50, the photocurrent increases almost linearly with increasing Bi content; for Bi50 to Bi100, the photocurrent instead decreases. To exclude any surface limitation (due to slow charge transfer or surface recombination), the photocurrent was also measured in KPi with added H_2O_2 as a hole scavenger. The hole scavenger photocurrent trend is similar to that in KPi (Fig. 3b), with a Bi50 film showing the highest photocurrent of up to 1.82 mA cm^{-2} at 1.23 V *vs.* RHE.

The charge transfer and separation efficiencies can be calculated from the photocurrent density with and without a hole scavenger (definition and calculation steps are described in the ESI†). The transfer efficiency (η_{trans}) of all compositions is shown in Fig. S10† and the overall trend at 1.23 V *vs.* RHE is shown in Fig. 3c. It is interesting to note that the charge transfer efficiencies of all Bi/Fe mixed vanadate films are more or less

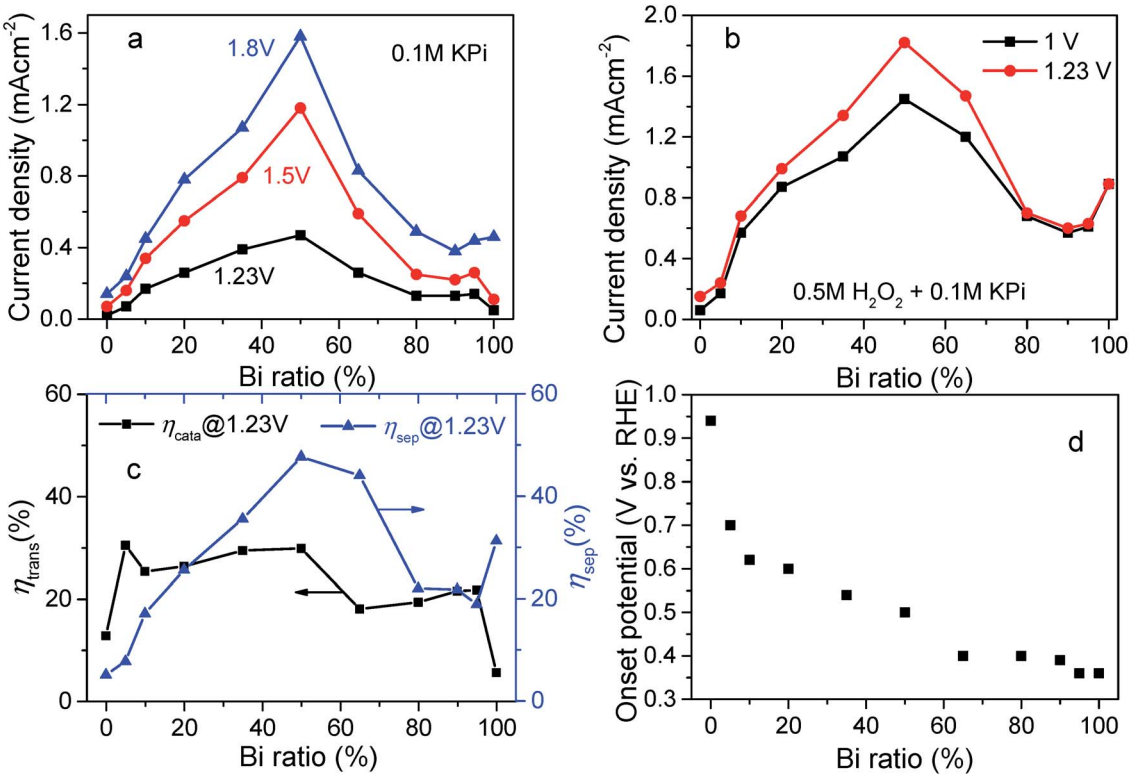

Fig. 3 (a) Photocurrent as a function of Bi ratio for all compositions, measured in 0.1 M KPi buffer (pH = 7) (a) and in 0.5 M H_2O_2 + 0.1 M KPi (b) under back-side illumination. (c) Charge transfer efficiency (η_{trans}) and separation efficiency (η_{sep}) at 1.23 V *vs.* RHE as a function of Bi ratio. (d) Onset potential taken from chopped current–voltage curves in KPi buffer.

constant and higher than those of pure $FeVO_4$ and $BiVO_4$ over the whole potential range. This is in good agreement with the observation that mixed vanadates have higher catalytic activity than a single metal vanadate.[15,17,19] In addition, a closer look at the trend shows that the η_{trans} of the films with higher Fe content (Bi5 to Bi50) is slightly higher than those of the Bi rich films (Bi65 to Bi100). We attribute this to the higher catalytic activity of Fe sites for oxygen evolution as compared to Bi. Indeed, the dark water oxidation current of $FeVO_4$ and Bi50 films is higher than that of $BiVO_4$ (Fig. S11†).

Since the J_{abs} values of all films are relatively close to each other (Fig. S6†), the charge carrier separation efficiency (η_{sep}) (Fig. 3c and S12†) follows a similar trend to the hole scavenger photocurrent. The incorporation of Bi/Fe at around a 1 : 1 ratio (*i.e.*, Bi50) results in an optimal charge separation. The η_{sep} of Bi50 at 1.23 V *vs.* RHE is 10-fold and 1.7-fold higher as compared to that of $FeVO_4$ and $BiVO_4$, respectively. It is therefore clear that the photocurrent improvement in the mixed Bi–Fe-vanadate films can be mainly attributed to the more efficient charge carrier separation.

The much higher η_{sep} can be explained by the formation of $FeVO_4$ and $BiVO_4$ heterojunctions with favorable band alignment to facilitate efficient charge carrier separation.[23] As the two vanadates are homogeneously distributed, indeed the 1 : 1 ratio is expected to be optimal to ensure enhanced charge separation at all parts of the film. A $BiVO_4$/$FeVO_4$ heterojunction in a 1 : 1 ratio has also been reported to obtain the highest photocatalytic activity for pollutant degradation,[30] which agrees very well with our results and interpretation.

Electrical impedance measurements were performed to shed light on the charge transfer processes. The Nyquist plots for all compositions derived from EIS measurements under illumination are shown in Fig. S13.† The different radii of semicircles can reflect the overall resistance. It is clear that Bi50 has the smallest semicircle; either increasing or decreasing the Fe content only results in a larger radius of the semicircle. An equivalent circuit is shown in Fig. S14,† which is typically used for the reported heterojunction structure and porous electrodes (the electrospun films show some extent of porosity as evidenced by SEM images). Here, R_s is the serial resistance, C_{sc} is the space charge layer capacitance, R_{ct} is the charge transfer resistance and CPE is the constant phase element.[31–33] From $FeVO_4$ to Bi50, R_{ct} reduces with increasing Bi ratio; however R_{ct} increases again from Bi50 to $BiVO_4$. Such a trend similar to the changes of the semicircle radius in the Nyquist plot implies that Bi50 has the lowest charge transfer resistance, which can be properly explained with the presence of a $BiVO_4$/$FeVO_4$ heterojunction.

The heterojunction explanation is also supported by the trend in the onset potential as a function of Bi ratio. The addition of $BiVO_4$ to $FeVO_4$ leads to a dramatic onset potential drop from 0.94 V *vs.* RHE (Bi0, $FeVO_4$) to ~0.4 V *vs.* RHE (Bi80–Bi95) (Fig. 3d). The cathodic onset potential shift is a typical effect of the heterojunction, which has been reported in TiO_2,

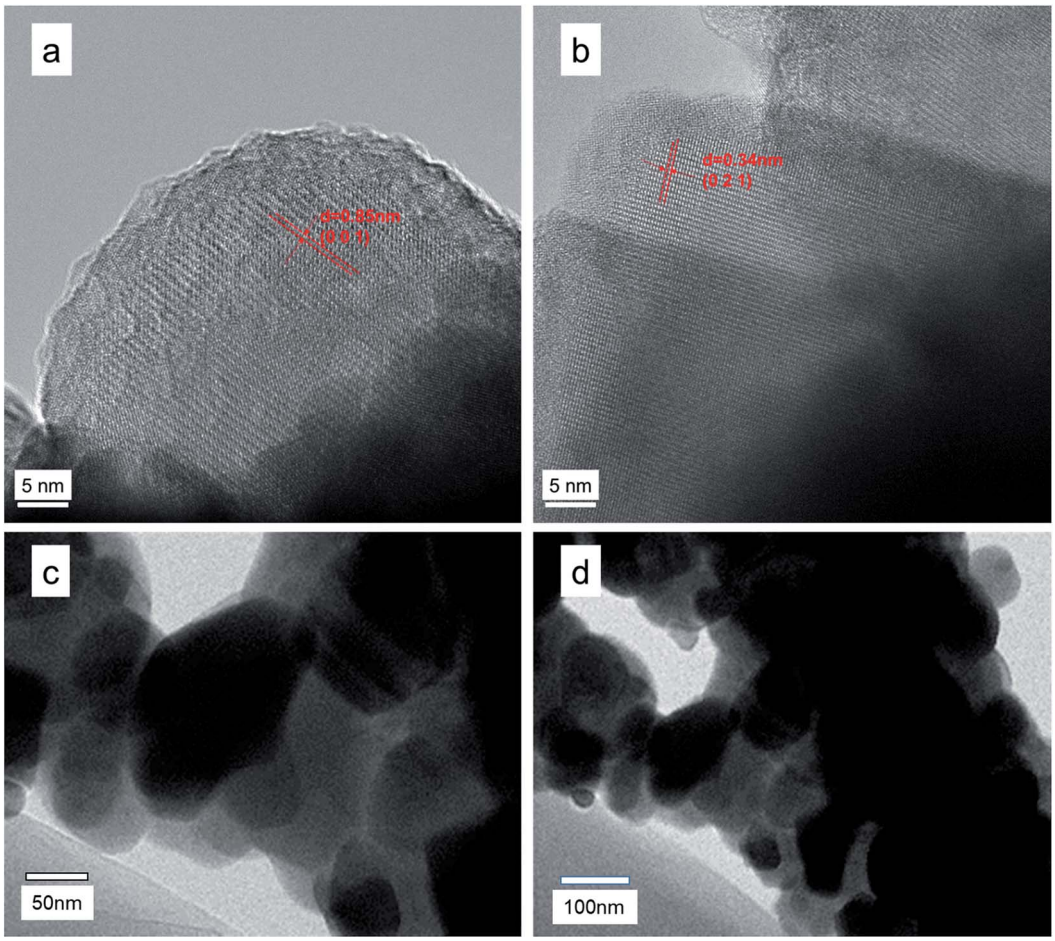

Fig. 4 (a) and (b) HRTEM images of the Bi50 sample at two different places, showing *d*-spacings of the $FeVO_4$ (001) and (021) planes to be 0.85 nm and 0.34 nm, respectively. (c) and (d) TEM images of the Bi50 sample at two different locations. Note the different scale-bars between the two images.

Fe_2O_3, and $BiVO_4$ photoanodes.[34–38] While elemental doping or surface passivation can also induce a cathodic onset potential shift, we have ruled out the presence of Bi or Fe doping in our mixed vanadates as no obvious peak shift was observed (see Fig. S2†) and the mixed vanadates show similar surface charge transfer efficiency (Fig. S10†). Further observations by SEM show that all films are composed of nanoparticles with similar morphologies (Fig. S15†). Capacitive current measurements

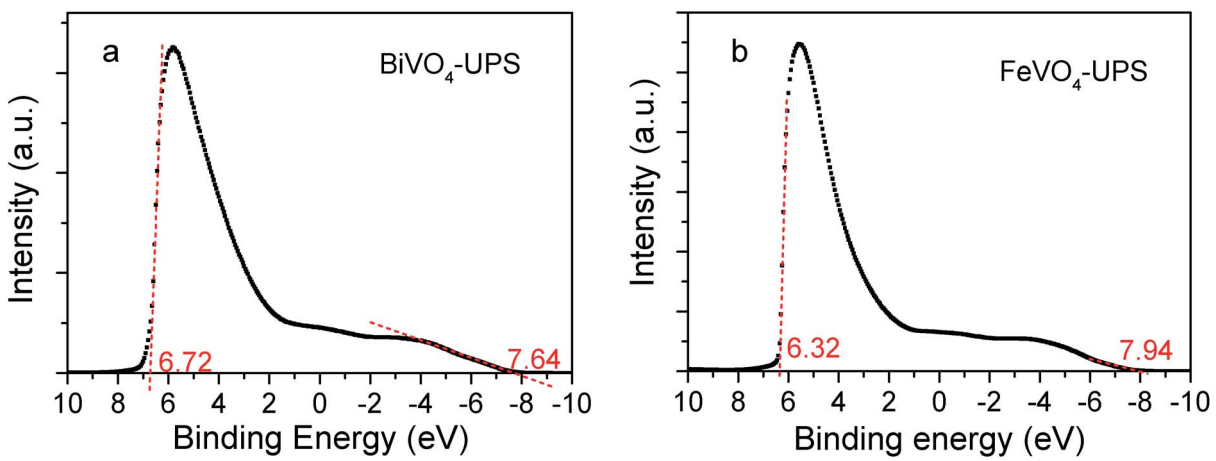

Fig. 5 UPS spectra of (a) $BiVO_4$ and (b) $FeVO_4$ with a bias of 10 eV. Secondary electron cut-off and valence band maximum positions have been indicated.

show no apparent trend of the electrochemical active surface area of all films (Fig. S16†). Cross-sectional view images also confirm similar particle sizes across the depth profile (~150–170 nm) for different compositions (Fig. S17†).

To further confirm the formation of a heterojunction, TEM and high resolution TEM (HRTEM) images of the Bi50 sample were taken as shown in Fig. 4. A clear phase contrast can be observed between the bright and dark regions (Fig. 4c and d), where the dark regions are surrounded by the bright regions. Clear lattice fringes can be observed in the bright regions, with *d*-spacings of 0.85 nm and 0.34 nm corresponding to the (001) and (021) planes of $FeVO_4$, respectively (Fig. 4a and b). The dark regions, however, do not show any clear fringes. To confirm the composition in the dark regions, Energy Dispersive X-ray Analysis (EDAX) was carried out at the sample locations shown in Fig. 4c and d, and the elemental mapping is shown in Fig. S18.† The dark regions are verified to be $BiVO_4$ particles while $FeVO_4$ particles (bright regions) are more dispersed. From the mapping images, the microscopic structure of $BiVO_4$ particles intimately surrounded by $FeVO_4$ particles can be proposed. This structure also explains why only the $FeVO_4$ phase can be clearly seen in the HRTEM images (bright regions), while the dark regions do not show lattice fringes due to the convolution between the $BiVO_4$ and $FeVO_4$ structure. This is further supported by the higher surface Fe/Bi ratio of the Bi50 film (2.2 as revealed from XPS, see Table S2†) as compared to the bulk Fe/Bi ratio of 1 (see Fig. 1a). Such an intricate structure shows clear evidence for the heterojunction, which enhances the charge carrier separation efficiency in the mixed vanadate films, particularly in the case of Bi50. A core–shell $BiVO_4/FeVO_4$ structure has indeed been reported to enhance charge separation.[23]

Mott–Schottky measurements were carried out to obtain the flat-band position of our films, which can be further used to estimate the Fermi level position. The flat-band potential of $BiVO_4$ and $FeVO_4$ is extrapolated to be ~0.13 V and ~0.72 V *vs.* RHE, respectively (Fig. S19†), which agree very well with reported values.[20,39] For a conclusive confirmation of band alignments, UPS was conducted and the spectra are presented in **Fig. 5**. The work function can be determined using the secondary electron cut-off. The position of the valence band maximum (E_V) with respect to the Fermi level (E_F) can be determined from the low kinetic energy cut-off of the spectrum.[39] As shown in **Fig. 5**, the work function for $BiVO_4$ and $FeVO_4$ can be determined to be 4.5 eV and 4.9 eV, respectively, while the E_V with respect to the E_F is determined to be 2.36 eV and 2.06 eV, respectively. Although the measured work function of $BiVO_4$ and $FeVO_4$ is slightly higher than the reported values ($BiVO_4$: 4.56 eV[39] and $FeVO_4$: 5.1 eV),[20] the difference of the work function position is definitely clear. The band alignments of $BiVO_4$ and $FeVO_4$, therefore, are depicted in Scheme 1. The conduction band position is calculated from the optical bandgap and valence band position. Scheme 1 clearly shows that $BiVO_4$ and $FeVO_4$ can form a heterojunction structure. Photogenerated holes can thus be more efficiently extracted for water oxidation due to larger band bending in the heterojunction, which is in agreement with the higher η_{sep} for Bi50 as compared with $BiVO_4$ and $FeVO_4$.

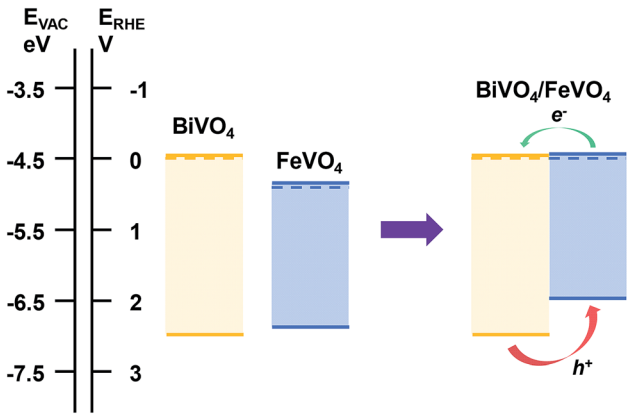

Scheme 1 Schematic diagram of band alignments of $BiVO_4$ and $FeVO_4$, confirming the heterojunction alignment. Note that the band bending at the interfaces is not depicted for simplicity.

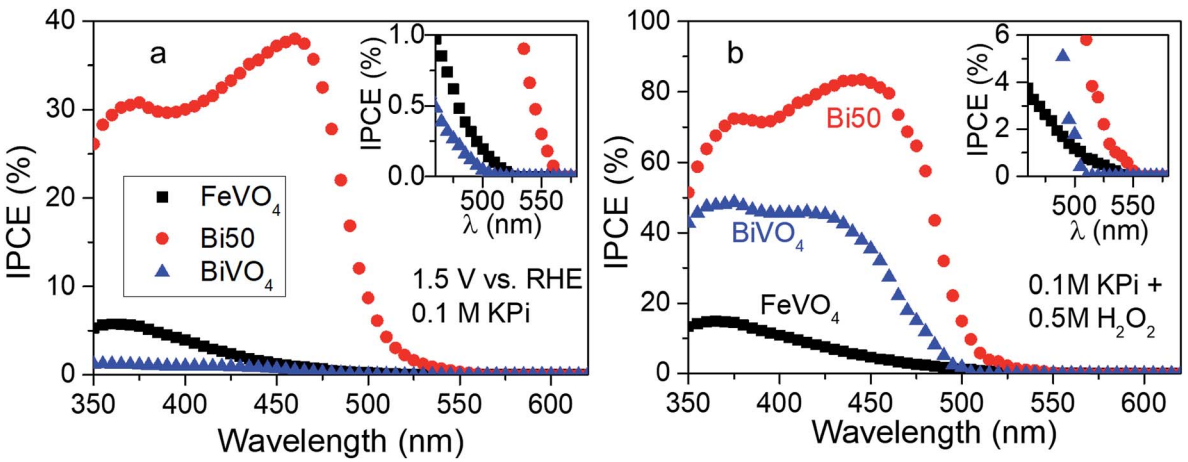

Fig. 6 IPCE of $FeVO_4$, Bi50 and $BiVO_4$ measured in (a) 0.1 M KPi and (b) 0.1 M KPi + 0.5 M H_2O_2 at 1.5 V *vs.* RHE. Both insets show the partially zoomed graphs to visualize the onset wavelength.

We also note that the optimal charge carrier separation efficiency in the Bi50 film can be caused by the improved charge carrier transport property (*i.e.*, carrier mobility). This is, however, unlikely to be the case. While we have no direct evidence of the carrier mobility in our electrospun films—time-resolved microwave conductivity (TRMC) measurements of our films are not possible since electrospinning the films on quartz (which is required for TRMC) results in mechanically unstable films—our previous study on sprayed mixed Bi–Fe-vanadates have shown that the carrier mobility continuously decreases with decreasing Bi content.[20]

Influence of the vanadate mixture on visible light photoactivity

Finally, we investigated the photoactivity of the films under different illumination wavelengths. The incident photon-to-current conversion efficiency (IPCE) curves of all films are shown in Fig. S20.† Although the absorption edge of $FeVO_4$ is ~600 nm, which is considerably longer than that of $BiVO_4$ (520 nm), the IPCE of $FeVO_4$ at wavelengths above 525 nm is negligibly small (~0) (**Fig. 6a**). The mismatch of the optical absorption onset and photoelectrochemical onset wavelength of $FeVO_4$ can be attributed to the low carrier mobility and indirect absorption energy loss in a long wavelength range.[20,40] Similar to the observation in UV-vis spectra, the IPCE at all wavelengths was enhanced for the mixed vanadates as compared with both $FeVO_4$ and $BiVO_4$ (Fig. S20†), with Bi50 showing the highest IPCE (**Fig. 6a**). Further IPCE measurements in H_2O_2 were carried out to better illustrate the onset wavelength for photoactivity (**Fig. 6b**). The Bi50 film clearly exhibits an extended PEC response to its absorption edge at 565 nm (corresponds to its indirect bandgap of 2.2 eV in Fig. 2c), while $FeVO_4$ and $BiVO_4$ displayed the same onset wavelength as in KPi (~520 nm, **Fig. 6b**). More direct evidence of the photo response of Bi50 at 550 nm is shown in Fig. S21.† It is clear that Bi50 generated measurable photocurrent under monochromatic illumination at 550 nm.

Since $FeVO_4$ and $BiVO_4$ show zero IPCE signal at wavelengths higher than 525 nm, the extended IPCE response for Bi50 can be attributed to the absorption in the $FeVO_4$ phase assisted by the presence of the $BiVO_4$/$FeVO_4$ heterojunction to improve charge separation as mentioned above. The equivalence of the optical onset and PEC onset wavelength for the Bi50 film therefore serves as evidence for a successful extension of the photoactivity in the mixed $BiVO_4$/$FeVO_4$ films.

Finally, Bi50 was measured in KPi at 1.5 V *vs.* RHE under illumination to investigate its stability. The photocurrent of the film continuously decreases in the 4000 s chronoamperometry measurement (Fig. S22a†). Therefore, a thin layer of CoPi was deposited by a well-established method for surface protection and the thickness of CoPi is estimated to be ~2 nm according to a report.[41] After CoPi deposition, other than the initial transient, the photocurrent stability is improved. The film is able to retain a photocurrent of ~0.6 mA cm^{-2} up to 4000 s (Fig. S22a†), implying that a thin layer CoPi can help protect the surface and improve the stability. This CoPi deposited Bi50 film was later used for oxygen evolution measurements due to its improved stability. The amount of oxygen generated was quantitatively recorded by gas chromatography. The faradaic efficiency for oxygen evolution was calculated to be ~88% (Fig. S23†).

Conclusions

A series of $Bi_xFe_{1-x}VO_4$ mixture mesoporous films was successfully fabricated by electrospinning. Instead of forming a solid solution, a mixed phase of $BiVO_4$ and $FeVO_4$ was detected from the X-ray diffraction patterns, and the indirect bandgap decreases with decreasing Bi/Fe atomic ratio. The mixed phase with an atomic ratio of Bi/Fe = 1, *i.e.*, Bi50, was found to have the optimum charge carrier transfer and separation efficiencies as compared with $BiVO_4$ and $FeVO_4$. Improved charge transfer efficiency was achieved due to a higher catalytic activity of the Fe and Bi cation mixture, while the enhanced charge separation was attributed to the homogeneously distributed $BiVO_4$/$FeVO_4$ heterojunction as observed from TEM. In addition, IPCE measurements revealed that the Bi50 composition demonstrates photoactivity up to ~560 nm, which is larger than that of pure $BiVO_4$ and consistent with the indirect bandgap of ~2.2 eV. Our work illustrates a simple yet successful strategy of forming a mixed phase heterojunction to expand light utilization as well as charge carrier transfer and separation efficiencies. Further improvement of the mixed phase films may be obtained through strategies well-reported in the literature, such as doping and nanostructuring.

Experimental

Preparation of $BiFeVO_4$ films

All the films were fabricated by electrospinning in a similar procedure from our previous report.[27] For one specific composition, $Bi_xFe_{1-x}VO_4$ ($0 \leq x \leq 1$), $0.06x$ mmol bismuth nitrate pentahydrate ($Bi(NO_3)_3 \cdot 5H_2O$, 98%, Sigma Aldrich), $0.03(1-x)$ mmol iron(III) acetylacetonate ($Fe(acac)_3$, 99.9%, Sigma Aldrich) and 0.03 mmol vanadium acetylacetonate ($VO(acac)_2$, 98%, Sigma Aldrich) were mixed so that the (Bi + Fe)/V ratio equals 1. The salt mixture was then dissolved in a mixed solvent containing 2 mL acetic acid (CH_3COOH, 99.7%, Sigma Aldrich), 2.5 mL absolute ethanol (CH_3CH_2OH, 99.5%, Merck) and 2.5 mL *N*,*N*-dimethylformamide ($HCON(CH_3)_2$, 99.8%, Sigma Aldrich). After adding 1200 mg polyvinylpyrrolidone (PVP, $(C_6H_9NO)_n$, $M_w \sim 1\,300\,000$, Sigma Aldrich), the solution was then kept at room temperature with magnetic stirring overnight to obtain a viscous and homogeneous solution. The addition of PVP was done to obtain an appropriate solution viscosity for electrospinning.

The resulting solution was then used for electrospinning deposition. 4 mL prepared solution was sucked into a 16 cm diameter syringe. The syringe and the electrospinning needle (20G, 13 mm length) were connected with chemical resistant tubing (Tygon 2375, $1/16 \times 3/16''$). The setup is shown in Scheme S1.† Fluorine doped tin oxide (FTO) substrates (14 Ω cm^{-2}, Nippon Sheet Glass) were subjected to a standard cleaning procedure (sonicated 20 min each in soap water, deionized water,

acetone, deionized water and ethanol). After drying with nitrogen flow, the FTO substrates were placed at the center of the electrospinning stage (collection plate) partially wrapped with aluminum foil to allow contact between the FTO conductive side and the stage. During the electrospinning process, a voltage of 25 kV was applied between the needle and the collection plate at a distance of 12 cm. The deposition rate was controlled at 1.5 mL h^{-1} using the syringe pump. The deposition was carried out at room temperature at different time intervals, *i.e.*, 15, 30 and 45 min. All the films were finally annealed at 550 °C in air for 3 h. The samples were denoted by the Bi content, for example $Bi_{0.3}Fe_{0.7}VO_4$ can be denoted as Bi30.

Characterization

The morphology of the films was observed by field emission scanning electron microscopy (FESEM) using a JEOL-7600F microscope. Energy dispersive X-ray spectroscopy (EDX) analysis was done with an Oxford INCA detector. For each composition, measurements were done in at least five different locations on the films to obtain an average value. The crystal structure of the films was measured by X-ray diffraction (XRD) using a Shimadzu thin film X-ray diffractometer (Cu Kα source). Optical absorption spectroscopy was measured on a UV-vis-NIR spectrophotometer (PerkinElmer, Lambda 950). For structural characterization, Transmission Electron Microscopy (TEM) analysis was performed using a JEOL 2100F transmission electron microscope. Powders carefully scratched from the film deposited on an FTO substrate were used for the TEM analysis. The powders were loaded onto the copper grid after sonicating in ethanol for 20 min to allow better dispersion. Energy Dispersive X-ray Analysis (EDAX) was performed for elemental mapping.

Photoelectrochemical (PEC) measurements were carried out on a CHI 660D workstation (CH Instruments Inc.). The mixed vanadate photoanodes were irradiated using a 150 W xenon solar simulator (67005, Newport Corp.) with a solar filter (KG 3) to achieve a measured light intensity of 1 sun (100 mW cm^{-2}). PEC measurements were performed in a PEC cell in a 3-electrode configuration, where the vanadate films were used as the anode, a Pt coil (3.6 cm^2) as the counter electrode, and an Ag/AgCl electrode (KCl 3 M solution) as the reference electrode. The PEC performance of the photoanodes were measured in a potassium phosphate buffer electrolyte (0.1 M KPi, pH = 7). The illuminated area on the photoanodes is fixed at 0.125 cm^2. Unless stated, all the PEC and IPCE measurements were performed under back-side illumination. Potential conversion to the reversible hydrogen electrode (RHE) scale was calculated using the equations below.

$$E_{RHE} = E_{Ag/AgCl} + E^0_{Ag/AgCl} + 0.0591 \times pH \quad (1)$$

where $E^0_{Ag/AgCl} = 0.21$ V *vs.* NHE at 298 K.

For PEC measurements with a hole scavenger, 0.5 M hydrogen peroxide (H_2O_2, 30% w/w in H_2O, Sigma Aldrich) was added to the KPi buffer solution. Incident photon-to-current conversion efficiency (IPCE) measurements were carried out using a combination of a xenon lamp (MAX-302, Asahi Spectra Co. Ltd.) and a monochromator (CMS-100, Asahi Spectra Co. Ltd.) from 350 to 620 nm wavelength. The IPCE values can be calculated using eqn (2).

$$\mathrm{IPCE}(\%) = \frac{1240(\mathrm{V\ nm}) \times \text{photocurrent density}(\mathrm{mA\ cm^{-2}})}{\text{incident light power density}(\mathrm{mW\ cm^{-2}}) \times \text{wavelength}(\mathrm{nm})} \quad (2)$$

Electrochemical active surface area (ECSA) measurements were performed using the same configuration as the PEC measurements, but without any irradiation (*i.e.*, in the dark). The potential was swept between 0 V to 0.6 V *vs.* Ag/AgCl at different scan rates (20, 50, 100, 150, 200, and 300 mV s^{-1}). The films were masked with tape to leave a fixed area (0.283 cm^2) for electrical contact. More details of the ECSA measurements can be found in other reports.[42,43] Electrical impedance spectroscopy (EIS) and Mott–Schottky measurements were conducted on an Autolab potentiostat (Metrohm-Autolab, AUT 83285) in a three electrode configuration using 0.1 M KPi solution. All the films were masked with tape to leave the same contact area (0.283 cm^2).

X-ray photoelectron spectroscopy (XPS) and ultraviolet photoelectron spectroscopy (UPS) measurements were conducted on the same VG ESCALAB 2201-XL instrument (operation condition $<5 \times 10^{-10}$ mbar) equipped with a monochromatic Al Kα (1486.7 eV) X-ray source and a He I discharge lamp (21.2 eV) UV source.

A stability test was carried out in KPi at an applied potential of 1.5 V *vs.* RHE for both untreated and CoPi deposited Bi50 films. CoPi was deposited by electrodeposition at 1.5 V *vs.* RHE for 60 s using 0.1 M KPi electrolyte containing 0.5 mM $Co(NO_3)_2$. A two-compartment electrochemical cell divided by an ion exchange membrane was used for the gas evolution test. The CoPi-Bi50 film was subject to 1.5 V *vs.* RHE in 0.1 M KPi under AM1.5 illumination. The amount of O_2 evolved was detected using a gas chromatograph (GC) (Agilent 7890A).

Conflicts of interest

There are no conflicts to declare.

Acknowledgements

Financial support by a Singapore Ministry of Education (MOE) Tier 2 grant (MOE2016T21030) is gratefully acknowledged. The authors thank Marlene Lamers for her assistance with the TRMC measurements.

References

1 Y. Pihosh, I. Turkevych, K. Mawatari, J. Uemura, Y. Kazoe, S. Kosar, K. Makita, T. Sugaya, T. Matsui, D. Fujita, M. Tosa, M. Kondo and T. Kitamori, *Sci. Rep.*, 2015, **5**, 11141.
2 F. A. Fatwa and P. B. Sean, *J. Phys. D: Appl. Phys.*, 2017, **50**, 193002.

3 J. E. Yourey and B. M. Bartlett, *J. Mater. Chem.*, 2011, **21**, 7651–7660.
4 I.-S. Cho, C. H. Kwak, D. W. Kim, S. Lee and K. S. Hong, *J. Phys. Chem. C*, 2009, **113**, 10647–10653.
5 M. Kölbach, I. J. Pereira, K. Harbauer, P. Plate, K. Höflich, S. P. Berglund, D. Friedrich, R. van de Krol and F. F. Abdi, *Chem. Mater.*, 2018, **30**, 8322–8331.
6 K. J. McDonald and K.-S. Choi, *Chem. Mater.*, 2011, **23**, 4863–4869.
7 N. Guijarro, P. Bornoz, M. Prévot, X. Yu, X. Zhu, M. Johnson, X. Jeanbourquin, F. Le Formal and K. Sivula, *Sustainable Energy Fuels*, 2018, **2**, 103–117.
8 L. Zhou, Q. Yan, A. Shinde, D. Guevarra, P. F. Newhouse, N. Becerra-Stasiewicz, S. M. Chatman, J. A. Haber, J. B. Neaton and J. M. Gregoire, *Adv. Energy Mater.*, 2015, **5**, 1500968.
9 P. F. Newhouse, D. A. Boyd, A. Shinde, D. Guevarra, L. Zhou, E. Soedarmadji, G. Li, J. B. Neaton and J. M. Gregoire, *J. Mater. Chem. A*, 2016, **4**, 7483–7494.
10 C. D. Morton, I. J. Slipper, M. J. K. Thomas and B. D. Alexander, *J. Photochem. Photobiol., A*, 2010, **216**, 209–214.
11 S. K. Biswas and J.-O. Baeg, *Int. J. Hydrogen Energy*, 2013, **38**, 14451–14457.
12 M. Lamers, W. Li, M. Favaro, D. E. Starr, D. Friedrich, S. Lardhi, L. Cavallo, M. Harb, R. van de Krol, L. H. Wong and F. F. Abdi, *Chem. Mater.*, 2018, **30**, 8630–8638.
13 Y. Nakabayashi, M. Nishikawa and Y. Nosaka, *J. Appl. Electrochem.*, 2016, **46**, 9–16.
14 Z. Ding, Y. Fu, Z. Xie and Z. Li, *Mater. Lett.*, 2011, **65**, 460–463.
15 H. Liu, R. Nakamura and Y. Nakato, *ChemPhysChem*, 2005, **6**, 2499–2502.
16 H. Liu, A. Imanishi, W. Yang and Y. Nakato, *Electrochim. Acta*, 2010, **55**, 4130–4136.
17 H. Liu, R. Nakamura and Y. Nakato, *Electrochem. Solid-State Lett.*, 2006, **9**, G187–G190.
18 Y. Murakami, M. Ikarashi, M. Hashizume, A. Y. Nosaka and Y. Nosaka, *Electrochem. Solid-State Lett.*, 2008, **11**, H42–H46.
19 G. Bera, V. R. Reddy, P. Mal, P. Das and G. R. Turpu, *AIP Conf. Proc.*, 2018, **1953**, 080026.
20 M. Zhang, Y. Ma, D. Friedrich, R. van de Krol, L. H. Wong and F. F. Abdi, *J. Mater. Chem. A*, 2018, **6**, 548–555.
21 M. Lamers, S. Fiechter, D. Friedrich, F. F. Abdi and R. van de Krol, *J. Mater. Chem. A*, 2018, **6**, 18694–18700.
22 A. P. Grosvenor, B. A. Kobe, M. C. Biesinger and N. S. McIntyre, *Surf. Interface Anal.*, 2004, **36**, 1564–1574.
23 M. Balamurugan, G. Yun, K.-S. Ahn and S. H. Kang, *J. Phys. Chem. C*, 2017, **121**, 7625–7634.
24 K. Lee, S. Shin, T. Degen, W. Lee and Y. S. Yoon, *Nano Energy*, 2017, **32**, 397–407.
25 Z. Liu, Q. Lu, E. Guo and S. Liu, *J. Nanopart. Res.*, 2016, **18**, 236.
26 C. D. Morton, PhD thesis, University of Greenwich, 2012.
27 R. P. Antony, P. S. Bassi, F. F. Abdi, S. Y. Chiam, Y. Ren, J. Barber, J. S. C. Loo and L. H. Wong, *Electrochim. Acta*, 2016, **211**, 173–182.
28 Y. Liu, Y. Guo, L. T. Schelhas, M. Li and J. W. Ager, *J. Phys. Chem. C*, 2016, **120**, 23449–23457.
29 J. Yang, D. Wang, X. Zhou and C. Li, *Chem.–Eur. J.*, 2013, **19**, 1320–1326.
30 J. Li, W. Zhao, Y. Guo, Z. Wei, M. Han, H. He, S. Yang and C. Sun, *Appl. Surf. Sci.*, 2015, **351**, 270–279.
31 J. Bisquert, *Phys. Chem. Chem. Phys.*, 2000, **2**, 4185–4192.
32 L. Zhang, E. Reisner and J. J. Baumberg, *Energy Environ. Sci.*, 2014, **7**, 1402–1408.
33 X. Shi, I. Herraiz-Cardona, L. Bertoluzzi, P. Lopez-Varo, J. Bisquert, J. H. Park and S. Gimenez, *Phys. Chem. Chem. Phys.*, 2016, **18**, 9255–9261.
34 H. Jung, S. Y. Chae, C. Shin, B. K. Min, O.-S. Joo and Y. J. Hwang, *ACS Appl. Mater. Interfaces*, 2015, **7**, 5788–5796.
35 S. J. A. Moniz, J. Zhu and J. Tang, *Adv. Energy Mater.*, 2014, **4**, 1301590.
36 S. Bai, H. Chu, X. Xiang, R. Luo, J. He and A. Chen, *Chem. Eng. J.*, 2018, **350**, 148–156.
37 S. Ho-Kimura, S. J. A. Moniz, A. D. Handoko and J. Tang, *J. Mater. Chem. A*, 2014, **2**, 3948–3953.
38 Q. Peng, J. Wang, Z. Feng, C. Du, Y. Wen, B. Shan and R. Chen, *J. Phys. Chem. C*, 2017, **121**, 12991–12998.
39 J. Resasco, H. Zhang, N. Kornienko, N. Becknell, H. Lee, J. Guo, A. L. Briseno and P. Yang, *ACS Cent. Sci.*, 2016, **2**, 80–88.
40 J. Feng, Z. Wang, X. Zhao, G. Yang, B. Zhang, Z. Chen and Y. Huang, *J. Phys. Chem. C*, 2018, **122**, 9773–9782.
41 C. Zachäus, F. F. Abdi, L. M. Peter and R. van de Krol, *Chem. Sci.*, 2017, **8**, 3712–3719.
42 J. Kibsgaard and T. F. Jaramillo, *Angew. Chem., Int. Ed.*, 2014, **53**, 14433–14437.
43 B. K. Kang, G. S. Han, J. H. Baek, D. G. Lee, Y. H. Song, S. B. Kwon, I. S. Cho, H. S. Jung and D. H. Yoon, *Adv. Mater. Interfaces*, 2017, **4**, 1700323.